JOURNAL OF GEOPHYSICAL RESEARCH, VOL. 102, NO. A10, PAGES 22,155–22,168, OCTOBER 1, 1997

Nonguiding center motion and substorm effects in the magnetotail

Richard L. Kaufmann, Ioannis D. Kontodinas, Bryan M. Ball, and Douglas J. Larson

Department of Physics, University of New Hampshire, Durham

Abstract. Thick and thin models of the middle magnetotail were developed using a consistent orbit tracing technique. It was found that currents carried near the equator by groups of ions with anisotropic distribution functions are not well approximated by the guiding center expressions. The guiding center equations fail primarily because the calculated pressure tensor is not magnetic field aligned. The pressure tensor becomes field aligned as one moves away from the equator, but here there is a small region in which the guiding center equations remain inadequate because the two perpendicular components of the pressure tensor are unequal. The significance of nonguiding center motion to substorm processes then was examined. One mechanism that may disrupt a thin cross-tail current sheet involves field changes that cause ions to begin following chaotic orbits. The lowest-altitude chaotic region, characterized by an adiabaticity parameter $\kappa \approx 0.8$, is especially important. The average cross-tail particle drift is slow, and we were unable to generate a thin current sheet using such ions. Therefore any process that tends to create a thin current sheet in a region with κ approaching 0.8 may cause the cross-tail current to get so low that it becomes insufficient to support the lobes. A different limit may be important in resonant orbit regions of a thin current sheet because particles reach a maximum cross-tail drift velocity. If the number of ions per unit length decreases as the tail is stretched, this part of the plasma sheet also may become unable to carry the cross-tail current needed to support the lobes. Thin sheets are needed for both resonant and chaotic orbit mechanisms because the distribution function must be highly structured. A description of current continuity is included to show how field aligned currents can evolve during the transition from a two-dimensional (2-D) to a 3-D configuration.

1. Introduction

A companion paper [*Kaufmann et al.*, this issue] and *Larson and Kaufmann* [1996] (hereafter called LK96) describe the consistent orbit tracing (COT) technique used here. The procedure starts by picking magnetic and electric field models. Orbits of many groups of particles are traced in these fields to calculate the electric current each group carries. The groups then are combined so that ions and electrons in the full plasma carry the electric current needed to generate the preselected magnetic field.

The region studied is $-20\,R_E < x < -14\,R_E$, $0 < |z| < 2\,R_E$ in geocentric solar magnetospheric (GSM) coordinates. The field model is symmetric about the equatorial plane, $z = 0$. The standard magnetic field from LK96 was used for most of the calculations in this paper. The model suggested by *Birn et al.* [1975] and *Zwingmann* [1983] provided the dominant contribution to our standard model in the region of interest. Parameters were adjusted to give a characteristic current sheet thickness of about $0.7\,R_E$ and so that both the total cross-tail sheet current density and the adiabaticity parameter would be similar to those obtained in the $Kp = 4$ version of the *Tsyganenko* [1989] (T89) model. The adiabaticity parameter is defined by $\kappa^2 = R_{min}/\rho_{max}$ [*Büchner and Zelenyi*, 1989], where R_{min} is the minimum magnetic field line radius of curvature and ρ_{max} is the maximum particle gyroradius. Both R_{min} and ρ_{max} are found at $z = 0$. A dipole and the *Tsyganenko and Usmanov* [1982] ring current model produced the dominant magnetic fields at lower altitudes.

The output from the COT analysis is a three-dimensional (3-D) velocity distribution function $f(\mathbf{r}, \mathbf{v})$ for each spatial box. The boxes are $\Delta z = 0.03$ to $0.1\,R_E$ wide in the z direction and $\Delta x = 0.5$ or $1\,R_E$ wide in the x direction. Only one wide box was used in the y direction, and the model is referred to as two dimensional because there is very little y dependence in the region of interest. The calculated $f(\mathbf{r}, \mathbf{v})$ then were used to evaluate fluid parameters such as the mass density ρ, the bulk velocity $\mathbf{V}$, and the pressure tensor $\mathbf{P}$.

Ion orbits in the neutral or inner plasma sheet region deviate markedly from the spiral guiding center motion that is typical of the outer plasma sheet and the radiation belts. Nonguiding center orbits have been studied by many groups. Previous studies were summarized by *Kaufmann et al.* [this issue] and by LK96, so we will refer to these papers rather than repeating the summary.

The goal of section 2 is to find which bulk parameters are strongly dependent on nonguiding center properties of particle orbits in the middle magnetotail. It was shown why the full pressure tensor is needed near $z = 0$ rather than only the pressures parallel and perpendicular to the magnetic field. The calculated pressure tensor is not oriented along $\mathbf{B}$ in the weak field region near the equator. A region also exists in the model in which $\mathbf{P}$ is nearly field aligned but the perpendicular pressure is not the same in all azimuthal directions around a field line.

In section 3 the results from the nonguiding center study are applied to substorm problems. It is concluded that cross-tail current

Paper number 97JA01986.
0148-0227/97/97JA-01986$09.00

may be disrupted in a region which is initially dominated by Speiser particles [*Speiser*, 1965]. Speiser particles follow spiral guiding center orbits while they are well away from $z = 0$. These particles carry cross-tail current very efficiently at $|z| < z_0$ where they meander one or more times across the equatorial plane. The location $z = z_0$ is the point at which the z component of the particle's gyroradius is equal to the particle's distance from the equatorial plane. This thickness parameter is defined by $z_0 = mv/[qB_{xy}(z_0)]$, where $B_{xy}^2 = B_x^2 + B_y^2$, m is the particle mass, v is the velocity, and q is the charge.

One specific disruption process involves a thin current sheet region in which the thickness and/or B_z changes until most current carriers have an adiabaticity parameter near $\kappa = 0.8$. Most particles with κ near 0.8 suffer rapid chaotic changes in orbital properties each time they interact with the neutral sheet, so the ions do not follow Speiser orbits for even a single interaction. We were unable to generate a consistent thin current sheet using ions with κ near 0.8. The next chaotic region at $\kappa = 0.4$ was found to support a thin current sheet.

Particles can remain on Speiser orbits and drift rapidly across the tail in a thin current sheet when their average κ parameter is near a resonant value such as 0.5. Here current disruption can be produced by a decrease in the number of particles in a resonant region because particles already are drifting at their maximum cross-tail speed. The fewer particles per unit length of the tail are unable to support the lobe field. Finally, reasons for changes in plasma sheet thickness and the relationship of 2-D steady state COT results to a 3-D time dependent tail are discussed.

2. Nonguiding Center Effects

The relatively thick standard model from LK96 will be used in this section. A uniform 0.3 mV/m cross-tail electric field was included to produce earthward plasma drift. The COT method traces orbits of a group of particles with preselected initial energies starting from a point that was randomly selected within one of the spatial boxes. Particles are energized by the electric field because they also drift in the cross-tail direction.

The inner current sheet is of particular interest because the model magnetic field is too weak at $|z| < z_0$ to deflect ions through 90° back toward the equatorial plane. This section will show that the pressure tensor is oriented in directions that are unrelated to the magnetic field and that the strength of the cross-tail current deviates substantially from guiding center predictions in the inner current sheet. In the outer current sheet beyond about $|z| = 2z_0$, ions spiral around the magnetic field line direction, and the guiding center approximations are valid.

2.1. Nonguiding Center Particles

LK96 showed that nonguiding center magnetotail ion orbits can be divided into three classes according to the cross-tail current distribution that each carries. This separation depends on the points at which particles either mirror or are reflected back toward the equator. Figure 1a is the y-z projection of a small segment of a particularly simple nonguiding center trapped particle orbit. An ion that follows this figure eight shaped trajectory as it meanders back and forth across the equatorial plane carries positive j_y at $|z| > z_0$ and negative j_y at $|z| < z_0$. There is only a small net drift in the positive y direction for the full orbit shown yielding a small average drift velocity v_{gy}. The subscript g indicates that this orbit-averaged drift corresponds to the bounce-averaged drift velocity of guiding center particles. The large localized currents associated with motion in the positive direction at $|z| > z_0$ and negative direction at $|z| < z_0$ correspond to magnetization currents $j_{my} = nqv_{my}$, where n is the number density and q is the charge. The total cross-tail velocity is the sum of the magnetization and orbit-averaged velocities, $v_{my} + v_{gy}$.

A second class of particles mirrors in the outer current sheet, beyond $|z| = 2z_0$. These trajectories were called cucumber orbits by *Büchner and Zelenyi* [1989]. Figure 2 of LK96 shows particles following cucumber orbits. Finally, the ion in Figure 1b which mirrors far from $z = 0$ is on a Speiser orbit. Such particles carry most of their cross-tail current in the $+y$ direction at $|z| < z_0$ and produce the thinnest current sheets.

The solid curves in Figures 2a and 2b show the current distribution $j_y(x, z)$ carried in the region $-17\ R_E < x < -15\ R_E$, $0 < |z| < 2\ R_E$ by a group of 1000 protons that were randomly selected from an isotropic 5-keV Maxwellian parent distribution starting at $(x, y, z) = (-15.5, 0, 0)\ R_E$. Figures 2a and 2b show the current distribution as a function of z within a $\Delta x = 1\text{-}R_E$-wide x box. Although few of these 1000 trajectories were as simple as the one shown in Figure 1a, the group was dominated by particles that were trapped at $|z| < 2z_0 = 0.5\ R_E$ while in these x boxes. The pattern of negative j_y at $|z| < z_0$, positive j_y at $|z| > z_0$, and small j_y in the outer current sheet is typical of trapped particle groups [*Kaufmann and Lu*, 1993]. Runs also were carried out using smaller z boxes to examine the interesting nonguiding center region in more detail. Figures 2c and 2d are these expanded plots for a similar randomly selected group of ions.

The solid curves in Figures 3a and 3b show $j_y(x, z)$ in the $-19\ R_E < x < -17\ R_E$, $0 < |z| < 0.8\ R_E$ region for a group of 1000 protons selected from a 5-keV Maxwellian distribution that started at $(-9.05, 0, 2.05)\ R_E$ in the outer plasma sheet. Most of these particles follow Speiser orbits. Their typical current pattern is concentrated at $|z| < z_0 = 0.25\ R_E$ but often exhibits a minimum very close to $z = 0$. Finally, the solid curves in Figures 3c and 3d show $j_y(x, z)$ carried in the $-19\ R_E < x < -17\ R_E$, $0 < |z| < 2\ R_E$ region by ions and electrons in the combined plasma that was generated by the COT analysis. This current nearly equals the $j_y(x, z)$ required to generate the standard model magnetic field.

2.2. Guiding Center Particles

The guiding center drift equation for particles of species s is

$$\mathbf{j}_{s\perp} = \frac{\mathbf{B}}{B^2} \times \left[\nabla P_{s\perp} + \frac{P_{s\parallel} - P_{s\perp}}{B^2} (\mathbf{B} \cdot \nabla) \mathbf{B} \right] + n_s q_s \frac{\mathbf{E} \times \mathbf{B}}{B^2} + n_s m_s \frac{\mathbf{B}}{B^2} \times [(\mathbf{V}_s \cdot \nabla) \mathbf{V}_s] \quad (1)$$

where parallel and perpendicular components of the current $\mathbf{j}_s$ and pressure tensor $\mathbf{P}_s$ are taken with respect to the direction of the magnetic field $\mathbf{B}$. Equation (1) can be obtained by combining guiding center gradient, curvature, $\mathbf{E} \times \mathbf{B}$, polarization, and magnetization drift terms [*Parker*, 1957]. This expression was used to calculate electron current in the COT analysis. The term in (1) involving the bulk velocity $\mathbf{V}_s$ is the polarization drift and is small in this magnetotail model.

A generalized version of the steady state drift equation

$$\mathbf{j}_{s\perp} = \frac{\mathbf{B}}{B^2} \times \sum_{\beta=1}^{3} \frac{\partial P_{s,\beta\alpha}}{\partial x_\beta} + n_s q_s \frac{\mathbf{E} \times \mathbf{B}}{B^2} + n_s m_s \frac{\mathbf{B}}{B^2} \times [(\mathbf{V}_s \cdot \nabla) \mathbf{V}_s] \quad (2)$$

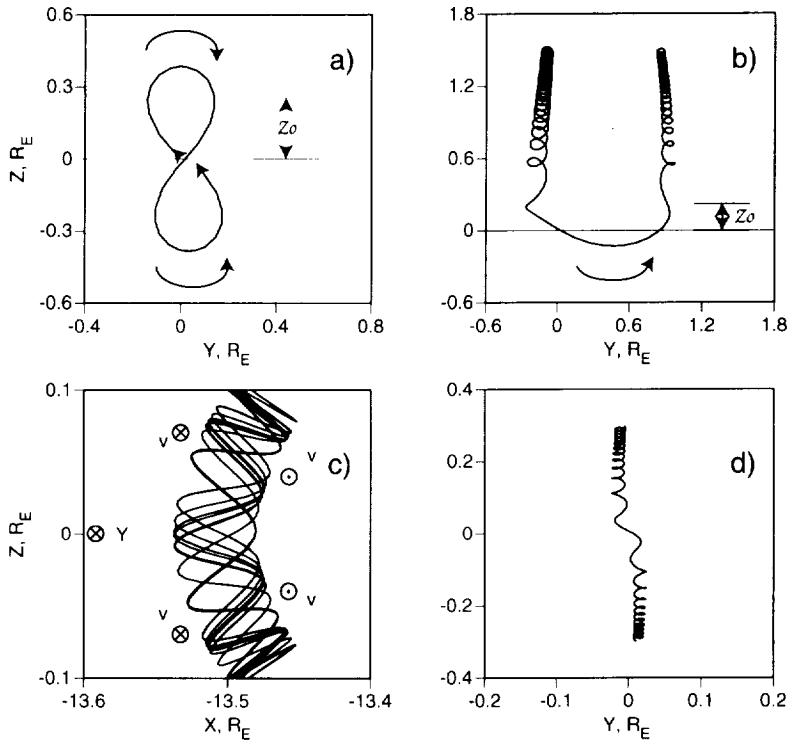

Figure 1. (a) A simple nonguiding center trapped particle orbit, (b) a Speiser orbit, (c) a guiding center orbit showing cross-tail magnetization currents, and (d) a guiding center orbit showing cross-tail drift motion.

is obtained by taking the cross product of the momentum equation [*Kaufmann et al.*, this issue, equation (6)] with **B** and dividing by B^2. The subscripts α and β refer to Cartesian components in GSM coordinates, and the sum is the divergence of the pressure tensor $\nabla \cdot \mathbf{P}_s$. Equation (2) follows directly from the Vlasov equation and should be valid for any group of particles in such a steady state plasma. Equation (2) reduces to (1) when $\mathbf{P}_s$ can be written in the form

$$\mathbf{P}_s = P_{s\perp}\mathbf{1} + (P_{s\parallel} - P_{s\perp})\,\mathbf{bb} \tag{3}$$

where **b** is a unit vector along **B** and **1** is the unit tensor. These approximations are valid for electrons but not for ions in the inner current sheet.

Figure 1c shows the x-z projection of a trapped particle that follows a guiding center orbit. Cross-tail magnetization current in the $-y$ direction near $z = 0$ is primarily given by the second $P_{s\perp}$ term in the square brackets in (1) and is physically produced by the crowding together of orbit segments on the concave side of the field line in Figure 1c. This particle is always moving in the $+y$ direction when it is farthest from $z = 0$, resulting in a positive j_{my}. Figure 1d is the y-z projection of a guiding center particle that mirrors far from the equatorial plane. The cross-tail motion of the particle's guiding center near $z = 0$ is produced primarily by magnetic field curvature drift or the $P_{s\parallel}$ term in (1).

Figures 1a - 1d illustrate some of the physical distinctions and some similarities between currents carried by guiding center and nonguiding center particles. Although the orbits in Figures 1a and 1c look quite different, both involve strong magnetization currents flowing in the $+y$ direction at the largest $|z|$ reached by the particles and in the $-y$ direction near $z = 0$. In both cases there is more back and forth motion than net drift, indicating that $v_{my} > v_{gy}$.

One important distinction is that the thickness parameter z_0 has special significance only for the nonguiding center ions. Many ions in the randomly selected groups of 1000 that produced the $j_y(x, z)$ distributions in Figures 2a - 2d are on trapped orbits that meander back and forth across $z = 0$ while remaining at $|z| < 2z_0$. The solid curves in Figures 2e and 2f show currents carried by a guiding center ion group. These particles also were started at $(-15.5, 0, 0)\ R_E$ with an isotropic distribution. An energy of 10 eV was used so the ions would have such a large κ that they follow guiding center orbits. Although the structure of negative j_y at $z = 0$ and positive j_y at large $|z|$ is qualitatively similar to that of trapped nonguiding center ions, the scale is much different. The z_0 parameter has no significance for guiding center particles because they follow spiral rather than meandering orbits. The mirror points of guiding center particles depend only upon their equatorial pitch angles and the magnetic field structure, not upon their energy or the energy dependent z_0 parameter.

Figures 2e and 2f show that both the dotted curve calculated using (1) and the dashed curve calculated using (2) produce good estimates of $j_y(x, z)$ for guiding center particles. The structure of $j_y(x, z)$ for these nearly guiding center particles was found to have a weak energy dependence. Figures 2e and 2f which used 10-eV protons have peaks at $z = 0.13\ R_E$. A similar plot was generated using 1-eV protons, and the peak moved to $0.10\ R_E$. If the definition of z_0 in section 1 is used, then $z_0 = 0.011$ and $0.0035\ R_E$ for 10-eV and 1-eV protons, respectively. Figures 2e and 2f therefore show that z_0 is not relevant for guiding center particles.

Equation (1) shows that $j_y(x, z)$ depends on temperature and density or pressure variations for guiding center particles. The density and temperature of particles vary as they drift in the electric field. However, in a 2-D model the distribution of particle energy as a function of x is independent of the magnitude of E_y, provided

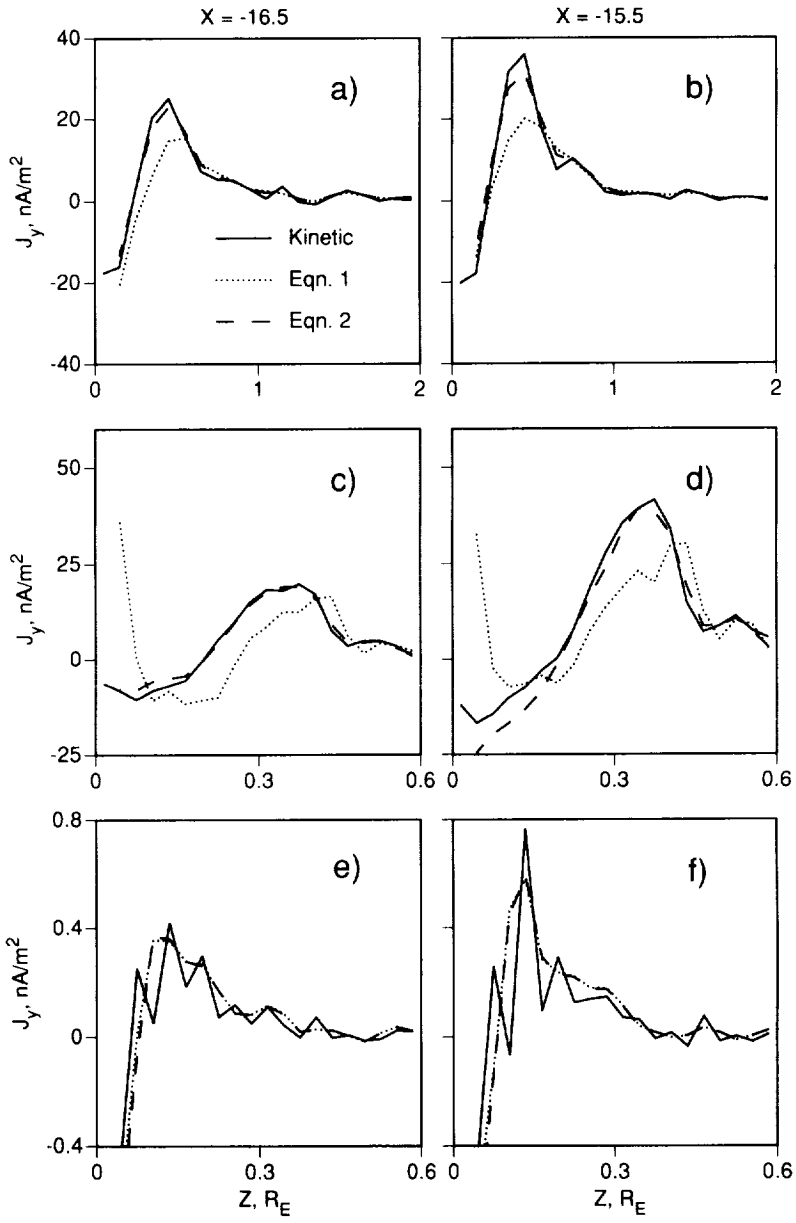

Figure 2. A comparison of j_y determined by integrating $f(\mathbf{r}, \mathbf{v})$ with the approximations given by equations (1) and (2) for two x boxes. Ions were injected with an isotropic distribution function at $(x, y, z) = (-15.5, 0, 0)$ R_E producing a group with many trapped ions. (a) and (b) The value j_y carried by 5-keV nonguiding center ions in the range $0 < |z| < 2$ R_E. (c) and (d) More detail in the $0 < |z| < 0.6$ R_E region. (e) and (f) are similar plots for 10-eV guiding center ions.

$E_y \neq 0$. For example, a particle that starts with 5 keV of energy at the equator at $x = -20$ R_E will be more energetic when it has drifted earthward and crosses the equator at $x = -14$ R_E in a uniform cross-tail field $E_y = 0.1$ mV/m. The particle gains energy because the magnetic field causes duskward drift. Doubling E_y to 0.2 mV/m doubles the earthward drift speed but does not change the cross-tail drift speed at a given x in the 2-D model. As a result, the particle in the larger E_y will reach $x = -14$ R_E twice as quickly, drift half as far in the y direction, and therefore gain the same energy in the 0.2 mV/m electric field as a particle that drifts to the same x in an 0.1 mV/m field. Similarly, the ratio of ion to electron energies remains constant if they $\mathbf{E} \times \mathbf{B}$ drift earthward and their cross-tail drift speed depends only on energy.

Figures 1b and 1d show that both guiding center and nonguiding center particles with mirror points near the Earth carry their strongest cross-tail current near $z = 0$. However, only the nonguiding center or Speiser particle current is confined to the region $|z| < 2z_0$, and only the nonguiding center particle $j_y(x, z)$ shows the resonant structure that will be described later. The solid curves in Figures 3e and 3f show the current carried by 10-eV guiding center protons that were injected at the same point as the 5-keV nonguiding center particles in Figures 3a and 3b. The qualitative similarity and difference in scales again is evident. The guiding center particles all have mirror points earthward of the (−9.05, 0, 2.05) R_E injection point so the distribution function is field aligned at $z = 0$ and $P_{||} > P_{\perp}$. As a result, the second term in (1) is dominant in the current sheet.

2.3. Breakdown of the Guiding Center Approximation

The solid curves in Figures 2, 3a, 3b, 3e, and 3f are nqV_y for single groups of 1000 ions each, where the bulk velocity $\mathbf{V}$ is cal-

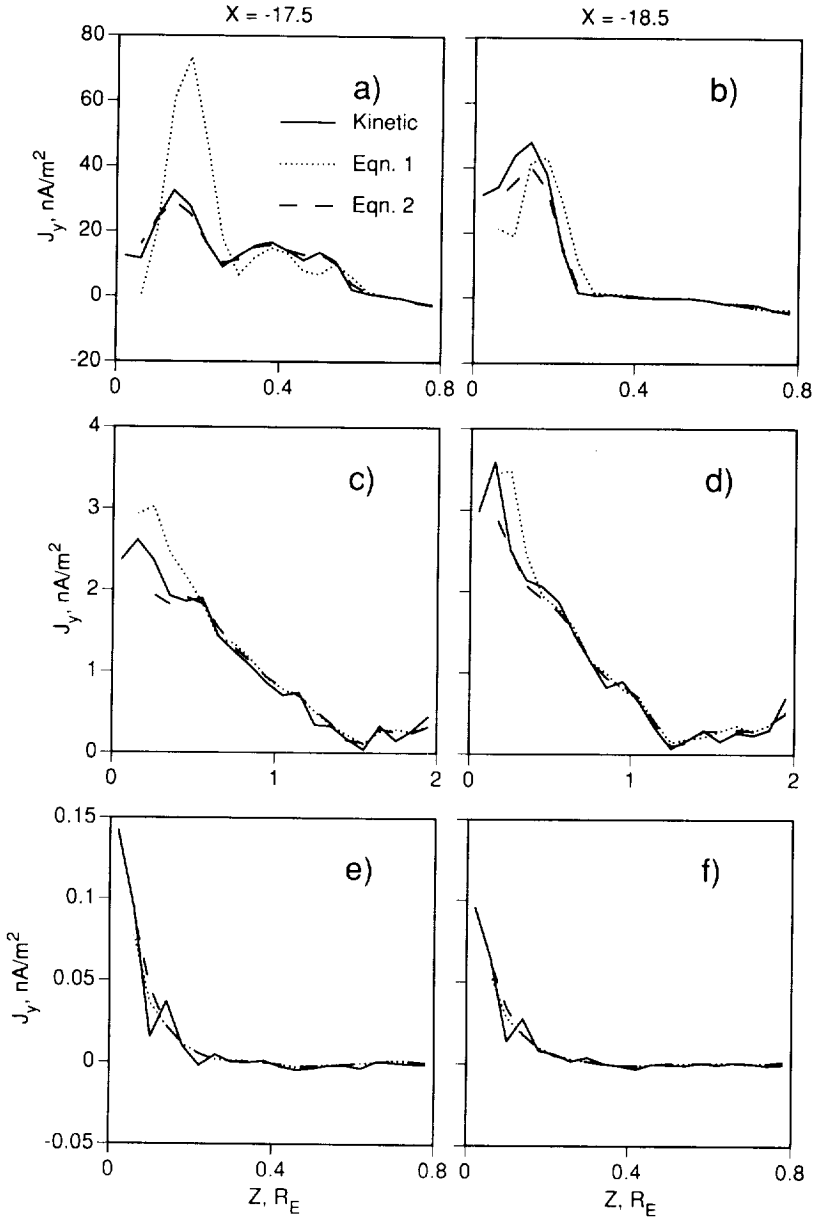

Figure 3. Similar to Figure 2 except (a) and (b) the 5-keV ions were injected at $(x, y, z) = (-9.056, 0, 2.053)$ R_E producing a group of Speiser particles. (c) and (d) Results from the combined consistent orbit tracing (COT) distribution function. (e) and (f) Similar to Figures 3a and 3b except 10-eV guiding center ions were used.

culated by integrating over the COT distribution functions $f_s(\mathbf{r}, \mathbf{v})$

$$V_{s,\alpha} = \frac{1}{n}\int v_\alpha f_s(\mathbf{r}, \mathbf{v})\, d^3v \tag{4}$$

The solid curves therefore show the actual current carried by all particles in the model plasma. The individual-pressure tensor [*Rossi and Olbert*, 1970]

$$P^{(s)}_{s,\alpha\beta} = m_s\int [v_\alpha - V_{s,\alpha}]\,[v_\beta - V_{s,\beta}]\, f_s(\mathbf{r}, \mathbf{v})\, d^3v \tag{5}$$

was also calculated by integrating over $f_s(\mathbf{r}, \mathbf{v})$. The superscript in (5) indicates that $\mathbf{P}^{(s)}_s$ is calculated in a frame moving at the bulk velocity of the species s rather than in the frame moving at the bulk speed of the entire plasma. This distinction is needed when looking at individual ion groups. Each ion group is treated as a separate species so that (4) and (5) give the bulk velocity and partial pressure tensor for that group. Since (2) requires taking numerical derivatives, the current calculated using this expression is less accurate than that shown by the solid curves. All of Figures 2 and 3 show good agreement between the kinetic results based on (4) and the dashed curves which are based on (2). The point at smallest $|z|$ has been omitted from all plots derived from (1) and (2) because the numerical derivatives have larger uncertainties at these end points.

The dotted curves in Figures 2 and 3 were calculated using (1) and show how much this guiding center expression deviates from the actual current carried by groups of anisotropic ions. These and similar figures for other particle groups showed that the three methods used to calculate $j_y(x, z)$ agree beyond approximately $|z|$ =

$2z_0 = 0.5\ R_E$. Causes of the differences at $|z| < 2z_0$ are described below. Figures 3c and 3d show that (1) and (2) give reasonably good estimates for j_y in the full consistent thick current sheet. This agreement is a result of the near isotropy of the combined ion distribution function near $z = 0$ in the thick model current sheet.

2.4. Pressure Tensor Elements

In any 1-D magnetotail model with $B_y = 0$ and $\partial/\partial x = \partial/\partial y = 0$, the only nonzero contributions to $\nabla \cdot \mathbf{P}$ are $\partial P_{zz}/\partial z$ and $\partial P_{xz}/\partial z$. The P_{zz} derivative produces particle forces in the z direction which balance the magnetic force associated with the increase of B as one moves from $z = 0$ to the lobes. The P_{xz} term provides the particle force that balances the magnetic force in the x direction.

Each element of $\mathbf{P}$ involves an integral of the distribution function times a product of two thermal velocities $w_\alpha w_\beta$, where $w_\alpha = v_\alpha - V_\alpha$. The bulk velocity V_α is small compared to the total particle speed v_α and to w_α for most particles in the quiet time model. Diagonal terms in the pressure tensor are largest because w_α^2 is positive at all velocities. Off-diagonal elements such as P_{xz} would be very small if w_x and w_z were uncorrelated since velocity space regions with positive and negative $w_x w_z$ products would nearly cancel. However, these two components can be highly correlated in a magnetized plasma.

As one simple example, consider a guiding center particle that mirrors near the Earth. When this particle is approaching the equatorial plane from its northern hemisphere mirror point, it will have an average $w_x < 0$ and $w_z < 0$. When the particle moves away from the equatorial plane toward its northern hemisphere mirror point, it will have an average $w_x > 0$ and $w_z > 0$. The $w_x w_z$ product therefore is usually positive near the equator and can produce a substantial off-diagonal pressure tensor element P_{xz}. The product is largest when w_x and w_z are approximately equal, which corresponds to the point at which $|B_x| = |B_z|$ for a field aligned guiding center particle. The physical significance of a large P_{xz} when $\partial/\partial z \gg \partial/\partial x$ or boxes are selected with $\Delta x \gg \Delta z$ is that particles which move from one z box to the next carry substantial x momentum. If $\partial P_{xz}/\partial z$ is large, then particles which enter one side of a z box and leave the other side will deposit net x momentum in the box. For the field-aligned particle example used above, particles in the northern hemisphere that are moving toward $z = 0$ tend to have a larger tailward x velocity when they enter a z box than when they leave it. Particles moving away from $z = 0$ tend to have a larger earthward x velocity when they leave a z box than when they enter it. In both cases the particle has gained momentum in the positive x direction while inside the z box. This requires an earthward force to be exerted on the particles. An equivalent physical picture is that a tailward centrifugal force is exerted by the particle as its guiding center moves along the curved magnetic field line.

Other pressure tensor elements also contribute to force balance in the 2-D model used here. The off-diagonal pressure tensor elements can be 10% or more of the diagonal elements for individual particle groups. Equation (2) shows that the x and z components of $\nabla \cdot \mathbf{P}$ contribute to j_y. The $\partial P_{zz}/\partial z$ term generally dominates over the $\partial P_{xz}/\partial x$ term in the z component of the divergence, just as for the 1-D case. However, $\partial P_{xx}/\partial x$ and $\partial P_{xz}/\partial z$ are comparable in the x component of the divergence in the interesting region near $z = 0$. For studies of j_x and j_z, it is the $\partial P_{yz}/\partial z$ term that is usually dominant in the 2-D model.

2.5. Normal Coordinates

Guiding center particles are most naturally described in a magnetic field oriented coordinate system. For a mirroring particle the positive and negative products of the guiding center thermal velocities parallel and perpendicular to $\mathbf{B}$ are equally likely, so the $w_\parallel w_\perp$ products and associated off-diagonal pressure tensor elements average to zero. The thermal velocities $w_{\perp 1}$ and $w_{\perp 2}$ along any two orthogonal directions perpendicular to $\mathbf{B}$ are highly correlated but are 90° out of phase for guiding center particles so the average $w_{\perp 1} w_{\perp 2}$ product and associated off-diagonal term in the pressure tensor also is zero. As a result, only the diagonal $P_\parallel$ and $P_{\perp 1} = P_{\perp 2} = P_\perp$ terms are nonzero as is assumed in (3).

Since $\mathbf{P}$ is a real symmetric tensor even for nonguiding center particles, it can always be diagonalized to give real eigenvalues and eigenvectors or normal coordinates. The three nonzero elements of $\mathbf{P}$ in the nonfield-aligned normal coordinate system will be called P_{I}, P_{II}, and P_{III}. There are two ways in which the assumptions that give (3) can be violated. First, it is possible that none of the normal coordinates of $\mathbf{P}$ is along $\mathbf{B}$. Second, even if one normal coordinate is nearly along $\mathbf{B}$ so that $P_{\mathrm{I}} = P_\parallel$, it is not necessary for the other two elements $P_{\mathrm{II}} = P_{\perp 1}$ and $P_{\mathrm{III}} = P_{\perp 2}$ to be equal.

Diagonalization and the calculation of normal coordinates relies upon accurate values of the off-diagonal elements. Distribution functions from the COT analysis produced the most reliable normal coordinates in the inner current sheet. LK96 showed that the ion temperature at the outer edge of the model current sheet is about half the temperature near $z = 0$. At large $|z|$ it is often found that the calculated velocity distribution function is zero in many of the higher velocity boxes because few of the ions which were traced had large enough velocities at this location to make contributions to the high-velocity boxes. Moment equations such as (4) and (5) give reliable values of the density, bulk velocity, and the large diagonal elements of the pressure tensor throughout the current sheet. However, the small off-diagonal elements of $\mathbf{P}$ are less reliable at large $|z|$.

Figure 4a shows the angle θ between $\mathbf{B}$ and the closest normal coordinate axis for trapped ion groups with the same starting parameters as those in Figure 2. Figure 4d is a similar plot for Speiser groups with the same starting parameters as those in Figure 3. Five runs using different randomly selected groups of 2000 ions each were used to produce the five curves that are superimposed in Figures 4a - 4f. This presentation was used to show the reliability with which normal axes can be calculated using the available $f(\mathbf{r}, \mathbf{v})$. The runs used 2000 ions each to produce more accurate off-diagonal elements and $\Delta z = 0.05$-R_E-wide z boxes in the $0 < |z| < 1\ R_E$ range to emphasize detail in the inner current sheet.

An inspection of the GSM components of the normal coordinate axes derived by diagonalizing $\mathbf{P}$ shows that near the equator the normal coordinates were consistently near the GSM x, y, and z axes. This feature is produced by the symmetry of the magnetic field model and of the injection scheme that was used. Since the magnetic field is symmetric about $z = 0$, distribution function information was folded about the equatorial plane. Particles contributed to the distribution function in the same spatial box whenever they were located at a distance $|z|$ either above or below the equator. Physically, this corresponds to starting pairs of particles, one at a point (x, y, z) and another at $(x, y, -z)$.

The magnetic field is in the z direction at $z = 0$ and points closer to the GSM z axis than to the other two GSM axes at $|z| < 0.1\ R_E$, the two smallest z boxes in Figure 4. Since the normal coordinates of $\mathbf{P}$ at $|z| < z_0 = 0.25\ R_E$ are nearly along the GSM x, y, and z axes, the angle θ is roughly equal to the angle between $\mathbf{B}$ and the z axis for the first two points on each curve in Figures 4a and 4d. The magnetic field points closer to the x GSM axis in all other z boxes. The angle θ is roughly equal to the angle between $\mathbf{B}$ and the x axis for the next three smallest z boxes in Figures 4a and 4d. The fifth z

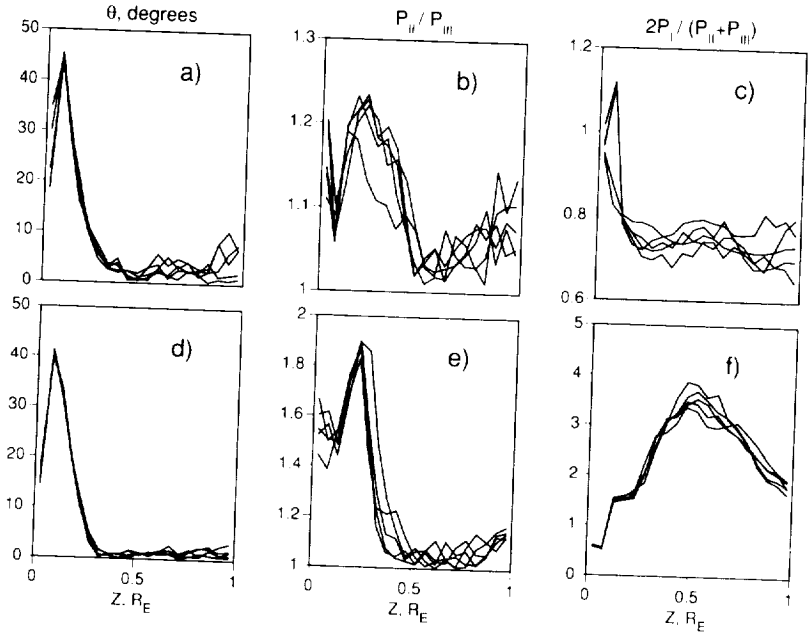

Figure 4. (a) and (d) The angle θ between **B** and the closest pressure tensor normal vector. (b) and (e) The ratio of the two diagonal pressure tensor elements associated with normal axes that are farthest from **B**. (c) and (f) A ratio that involves all diagonal pressure tensor elements. This ratio is $P_{II}/P_{\perp}$ if the first normal coordinate points along **B**. The ions in Figures 4a - 4c were injected at (−15.5, 0, 0) R_E producing a group of trapped ions and those in Figures 4d - 4f were injected at (−9.056, 0, 2.053) R_E producing a group of Speiser ions.

box extends to $|z| = z_o$. Beyond this point one of the normal coordinates of **P** points closer to **B** than to any of the GSM axes, so the pressure tensor has become field aligned. Figures 4a and 4d show that θ becomes very small, indicating that one of the normal coordinates is very close to **B**, somewhere in the range $z_o < |z| < 2z_o = 0.5\ R_E$.

To be more quantitative, recall that the 2-D model magnetic field is in the x-z plane. The x-z plane projection of one normal coordinate was found to point within about 1° of the magnetic field direction everywhere beyond $|z| = 1.5\ z_o$ for the Speiser group. This normal coordinate fluctuates by 2° to 3° out of the x-z plane. However, these small deviations in the y direction appear to be edge effects produced by particles entering and leaving an x box at different z locations. The y deviations become smaller as particle starting points are spread over larger regions to smooth out edge effects. Figure 4a shows that the trapped particle group also becomes field aligned near $|z| = 1.5\ z_o$. The increasing scatter in Figure 4a near $|z| = 1\ R_E$ shows that the pressure tensor elements are not accurate enough in this region to calculate reliable normal coordinates for the trapped particle group. The trapped particle results are inaccurate near and beyond 1 R_E because few particles in the group reach this far from $z = 0$.

Figures 4b and 4e show the ratio P_{II}/P_{III} where the elements have been ordered so that $P_{II} > P_{III}$. In the region $|z| > 1.5\ z_o$ where **P** is field aligned, P_{II} and P_{III} are the two perpendicular pressure elements. Comparing Figure 4a with Figure 4b and Figure 4d with Figure 4e shows that there is a region somewhere between z_o and $2z_o$ in which **P** is field aligned or θ is nearly zero but in which there is substantial perpendicular asymmetry ($P_{II} \neq P_{III}$). Beyond about $|z| = 2z_o$, **P** is both field aligned and symmetric about **B**. Here Figures 4b and 4e show that the average calculated P_{II}/P_{III} ratio deviates from one by no more than the scatter of points, indicating that this deviation can be explained by errors in determining the normal coordinates.

Figures 4c and 4f show $2P_{\perp}/(P_{II} + P_{III})$ which is $P_{II}/P_{\perp}$ when **P** is field aligned and symmetric about **B**. The qualitative behavior of the pressure ratios agrees with expectations for the orbit groups selected. Particles should have $P_{II} < P_{\perp}$ near their mirror or reflection points. Most particles in the generally trapped group (Figure 4c) are reflected in the region shown. The Speiser particles mirror beyond the region plotted in Figure 4. Their $P_{II}/P_{\perp}$ ratio (Figure 4f) is expected to increase through the ordinary mirror effect as particles move toward the equator as long as the magnetic moment μ is conserved. The Speiser particles become more nearly isotropic at the smallest $|z|$ where μ is not conserved. Although qualitative features can be understood, a quantitative analysis is difficult using the information in Figure 4. It must be recalled that each panel shows variations as z increases at a fixed x, not the variation seen when one moves along a field line. Particles located at $z = 1\ R_E$ in the thick model cross the equator 3 to 4 R_E tailward of the x box being studied.

To summarize this section, it was shown that the direction of **B** is almost irrelevant to the orientation of **P** at $|z| < z_o$ for groups that are dominated either by trapped or by Speiser particles. Section 3 describes a thin current sheet that was made using only Speiser particles. It therefore is not sufficient to calculate only P_{II} and $P_{\perp}$ in a thin current sheet when analyzing satellite measurements near $z = 0$. All elements of **P** are needed. For the cases studied, the calculated **P** consistently became field aligned somewhere in the region $z_o < |z| < 2z_o$. A small region was found extending beyond the point at which **P** became field aligned in which (1) and (3) are invalid because $P_{II} \neq P_{III}$ (Figures 4b and 4e). It was found that (1) and (3) can be used beyond $|z| = 2z_o$. These conclusions suggest that evaluating **P** may provide a way to determine whether a satellite is near $z = 0$ in a thin current sheet. If the observed **P** is not field aligned then the satellite is likely to be located at $|z| < 1.5\ z_o$. The test is not useful when **B** is nearly along a GSM axis since then it is not possible to distinguish between GSM-aligned and field-aligned orientations.

Figure 5 shows the same parameters that were plotted in Figure

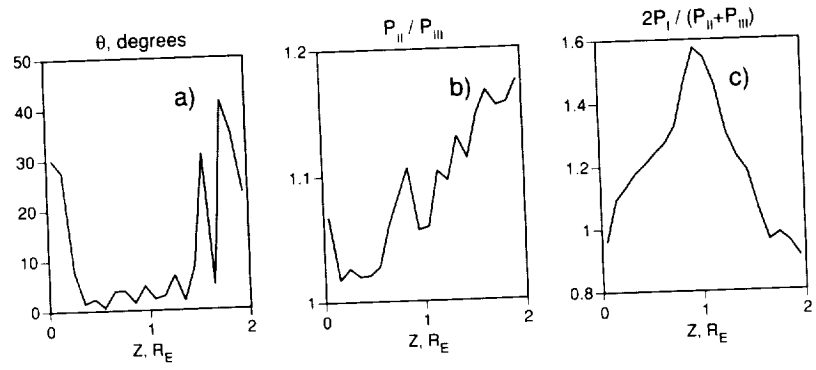

Figure 5. Similar to Figure 4 except using the combined COT distribution function. (a) The angle θ between **B** and the closest pressure tensor normal vector. (b) The ratio of the two diagonal pressure tensor elements associated with normal axes that are farthest from **B**. (c) A ratio that involves all diagonal pressure tensor elements. This ratio is $P_{II}/P_{\perp}$ if the first normal coordinate points along **B**.

4 but now for the final $f(\mathbf{r}, \mathbf{v})$ that was produced by summing ion groups to produce the thick COT model. Figure 5a shows that θ becomes small or **P** becomes field aligned near $|z| = 1.5\ z_o$. The full $0 < |z| < 2\ R_E$ range is plotted in Figure 5 to show that the normal coordinate determination fails so the calculated θ becomes erratic near $|z| = 1.5\ R_E$. The z boxes are twice as large in Figure 5 as in Figure 4. As a result, the θ variations very close to $z = 0$ are not well illustrated in Figure 5. However, the normal coordinates again are aligned with the GSM axes near $z = 0$. Figures 5b and 5c show that **P** is nearly isotropic and nearly symmetric in the region $|z| < z_o$ since P_I, P_{II}, and P_{III} are all nearly equal. A number of authors have shown that **P** must approach isotropy near $|z| = 0$ if $f(\mathbf{r}, \mathbf{v})$ is symmetric in an equilibrium current sheet [*Cole and Schindler*, 1972; *Rich et al.*, 1972; *Cowley*, 1978; *Nötzel et al.*, 1985; *Hill and Voigt*, 1992].

3. Substorm Effects

3.1. Kappa Dependence

The observation that thin current sheets often form before substorm onset suggests that nonguiding center effects may play a role in the substorm process. Orbits were classified in section 2 according to particle mirror or reflection points because this separation into trapped, cucumber, and Speiser orbits determines the basic shape of the cross-tail current distribution $j_y(x, z)$. Processes discussed in this section also depend on the dynamical characteristics of particle orbits. It is possible for a group of Speiser particles to be dominated by either resonant or chaotic orbits. The dominant dynamical characteristic of a group of particles depends on the κ parameter (section 1), which varies with both the ion energy and the current sheet thickness. The first and second orbital resonances

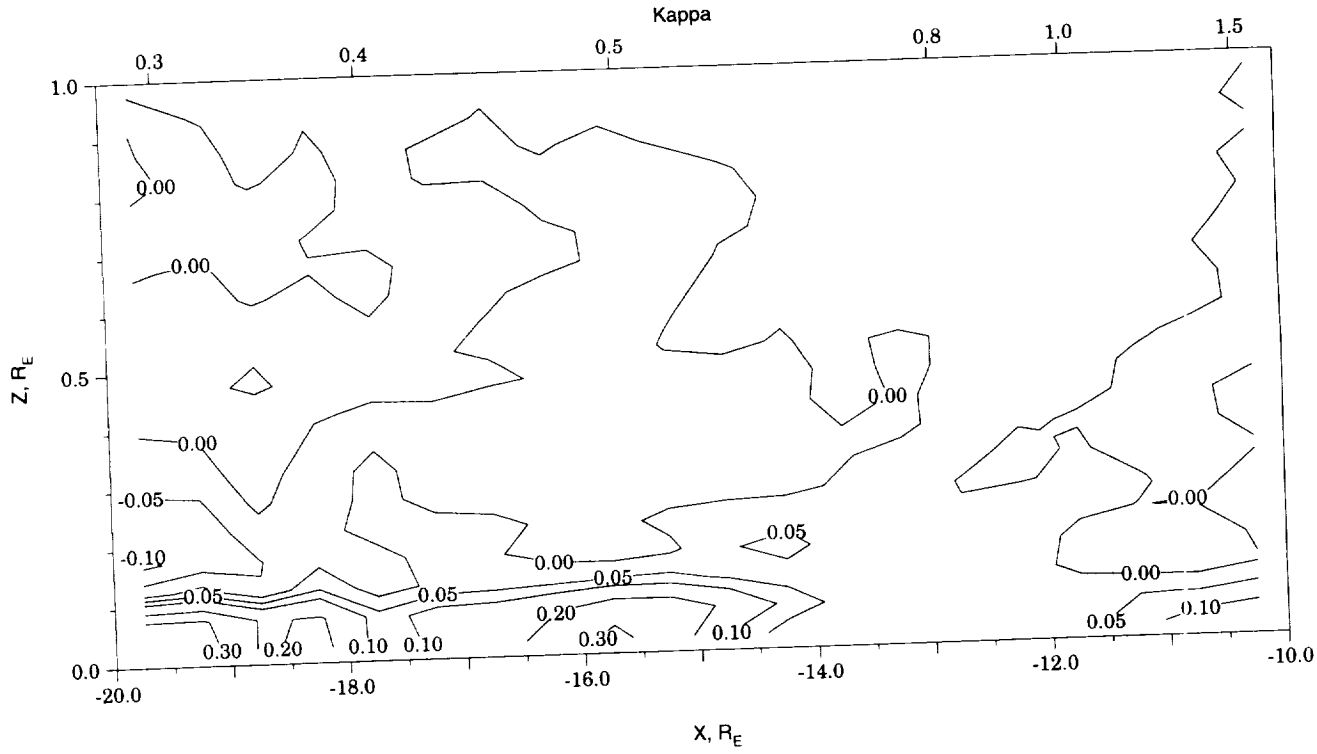

Figure 6. Contour plot of V_y/v_o, where V_y is the cross-tail bulk velocity and v_o is the total particle velocity, as a function of x and z for ion groups that are dominated by Speiser orbits. The κ values marked on the top axis are averages for particles that cross $z = 0$ at this x location.

appear near $\kappa = 0.5$ and $\kappa = 0.3$, respectively. Most particles in a group with $\kappa = 0.5$ cross the equatorial plane 2 times (Figure 1b), and most particles with $\kappa = 0.3$ cross the equator 3 times per current sheet interaction. Ions in a group with a resonant κ parameter leave the current sheet region with almost the same magnetic moments they had when they entered. Almost all resonant ions that enter the current sheet on Speiser orbits will also leave the current sheet on Speiser orbits. When κ is near 0.4 or 0.8, particles exhibit their most chaotic behavior. The mirror points of chaotic particles that leave the current sheet depend very sensitively upon all orbital parameters of the particles when they entered. An incident group of chaotic Speiser particles becomes thoroughly mixed between Speiser, trapped, and cucumber orbits.

Section 2 was based on studies of a thick quiet time current sheet. The characteristic magnetic field z scale length L_z was much larger than the thickness parameter z_0 (section 1) for 5-keV protons. Individual groups of particles had highly anisotropic distribution functions near $z = 0$, but the final consistent current sheet was nearly isotropic because the consistent thick model required a mixture of all orbit types. This section emphasizes results from a 2-D equilibrium model of a thin current sheet (A. Bhattacharjee, personal communication, 1996). A current sheet with thickness $L_z \approx z_0$ is important because it can be created using only Speiser particles. The resulting consistent thin current sheet has a highly anisotropic distribution function.

Figure 6 shows the most significant result obtained from studying thin current sheets. The plot shows contours of the parameter V_y/v_0, where V_y is the cross-tail ion bulk velocity and v_0 is the total ion velocity. Groups of monoenergetic 5-keV Speiser protons were started at $z = 2.5\ R_E$ along a number of field lines to prepare this plot. Monoenergetic ions were used because κ is energy dependent, and we wanted all ions in a group to have nearly the same κ. Ions drifted through the region of interest, but V_y was retained only in the one or two 0.5-R_E-wide x boxes nearest the point at which the ions first crossed $z = 0$. These runs used $\Delta z = 0.05$-R_E-wide z boxes, and 15 ion groups were traced to create Figure 6.

Note that V_y/v_0 in the $-16.0\ R_E < x < -15.5\ R_E$ x box exceeds 0.3 at $z = 0$, drops to 0.2 at $z = 0.1\ R_E$, and drops to zero at $z = 0.15\ R_E$. This concentration of current into a well-defined sheet at $|z| < z_0 = 0.1\ R_E$ is typical of Speiser orbits (Figures 1b, 3a, and 3b). The κ parameter defined in section 1 was determined by calculating the field line radius of curvature $\mathbf{R}/R^2 = -(\mathbf{B}\cdot\nabla)\mathbf{B}/B^2$ and the maximum ion gyroradius $\rho_{max} = mv_0/qB$ each time an ion crossed $z = 0$. The κ values shown at the top of Figure 6 are averages for all particles that crossed the equatorial plane at a given x and therefore refer to ions near $z = 0$. A particle that is located at $z = 1\ R_E$ in the $-16.0\ R_E < x < -15.5\ R_E$ x box will cross the equatorial plane 3 R_E tailward of this region and will have a different κ (Figure 6). The reason V_y/v_0 is so large near $z = 0$ in this particular x box is that $\kappa = 0.5$ is a resonant value. Almost all these ions remain on Speiser orbits throughout their current sheet interaction. The maximum value of V_y/v_0 for any one Speiser particle would be produced if the particle followed a semicircular path in the x-y plane with no bounce motion in the z direction. Such a particle would have $V_y/v_0 = 0.6$.

The $-13.5\ R_E < x < -12.5\ R_E$ x boxes in Figure 6 show the opposite extreme. Particles crossing $z = 0$ in this region have an average $\kappa = 0.8$, which corresponds to the most chaotic behavior. Although they started at $z = 2.5\ R_E$, the trajectories do not resemble typical Speiser orbits throughout even one current sheet interaction. The V_y/v_0 parameter is less than 0.03 at $z = 0$, and Figure 6 shows no evidence of a thin current sheet at this location.

The $-18.0\ R_E < x < -17.5\ R_E$ x box contains ions with an average $\kappa = 0.4$, which is the second chaotic region. Here V_y/v_0 at $z = 0$ drops to 0.07, and this parameter reaches zero slightly beyond $z = 0.1\ R_E$. Even though V_y/v_0 is small when $\kappa = 0.4$, Figure 6 shows current concentrated in a sheet at $|z| < z_0$. The second resonance takes place near $\kappa = 0.3$, which occurs in the $-20\ R_E < x < -19\ R_E$ x boxes. Here the V_y/v_0 parameter again exceeds 0.3, as it did at the first or $\kappa = 0.5$ resonance, and a thin very well defined current sheet is evident. Finally, the $-11\ R_E < x < -10\ R_E$ boxes show that thin current sheets can be produced by the large κ nearly guiding center particles.

The monoenergetic groups that were used to prepare Figure 6 were combined in a COT analysis. Groups with Maxwellian energy distributions also were run using the same $z = 2.5\ R_E$ starting points. Particles in the Maxwellian groups have a fairly wide distribution of κ values at any one location, producing a mixture of resonant and chaotic particles. It was easy to find either monoenergetic or Maxwellian groups that produced consistent current sheets near the resonant regions at $\kappa = 0.3$ and 0.5. Good models also could be produced near the $\kappa = 0.4$ region of chaotic orbits. When Maxwellian groups were used, the $\kappa = 0.4$ fits were almost as good as fits near the resonances. However, we were unable to create anything resembling a thin current sheet using either monoenergetic or Maxwellian particles with an average $\kappa = 0.8$. *Burkhart et al.* [1992] first noted this problem when injecting particles at large z in a 1-D tail model. The significance of this result is discussed below.

3.2. Disruption of Thin Current Sheets

Figure 6 shows that any process which uniformly changes κ will increase the average V_y of nonguiding center ions in one part of a thin current sheet and simultaneously decrease V_y somewhere else. A change in either the plasma sheet thickness or in B_z changes κ everywhere. Such a process may induce current disruption if κ approaches 0.8 in an initially thin region of the current sheet because particles with κ near 0.8 carry so little cross-tail current. A region that is initially thin is needed to cause disruption or current diversion by this nonguiding center mechanism because only thin sheets are composed of Speiser particles with a highly anisotropic $f(\mathbf{r}, \mathbf{v})$. Trapped particles also have a highly anisotropic $f(\mathbf{r}, \mathbf{v})$, but current sheets cannot be constructed using only trapped ions because the sign of the associated $j_y(x, z)$ reverses at $|z| = z_0$. The V_y/v_0 variations are much less striking than those shown in Figure 6, and $f(\mathbf{r}, \mathbf{v})$ is much more nearly isotropic when particles with different orbit types are mixed as in the thick current sheet described previously.

Since $\kappa \gg 1$ in the radiation belts and κ generally becomes small somewhere in the middle magnetotail [*Pulkkinen et al.*, 1992; *Kaufmann et al.*, 1993], there nearly always must be a region with $\kappa = 0.8$. Figure 6 shows weak cross-tail current in the $+y$ direction throughout a thick region when $\kappa = 0.8$ even though we were trying to generate a thin sheet. This illustrates the tendency of particles in a $\kappa = 0.8$ region to broaden any initially thin current sheet. We were able to generate reasonably good COT models of a thick current sheet with $\kappa = 0.8$, though the fits were more jagged than the fits with smaller κ shown by LK96 and *Kaufmann et al.* [this issue].

A problem arises because a certain sheet current density $K_y(x)$, which is $j_y(x, z)$ integrated through the thickness of the current sheet, is needed according to Ampere's law to produce the lobe field. A specific equilibrium lobe field is in turn required so that the outward magnetic force per unit area exerted by the lobe on the magnetopause balances the total inward force per unit area

exerted by the magnetosheath plasma and fields. *Kaufmann et al.* [this issue] concluded that when a current diversion loop forms, portions of the plasma sheet outside the loop will be accelerated in the tailward direction. The tailward force is generated because B_z decreases everywhere outside an intensifying current diversion loop. This decrease in B_z can reduce the earthward electromagnetic force $j_y B_z$ so that it becomes smaller than the tailward pressure force $\nabla \cdot \mathbf{P}$. This will cause a rapid stretching and thinning of portions of the current sheet [*Ohtani et al.*, 1992] and an associated decrease in κ. There may not be enough particles in the thinned plasma sheet to carry the required K_y if κ approaches 0.8, and therefore V_y becomes very small. This process could produce either secondary current disruption events or a spreading of the disruption region. The initial disruption at substorm onset is discussed below.

A second important feature of nonguiding center particles that is shown in Figures 1b and 6 is that the average cross-tail drift speed of Speiser particles near $z = 0$ in resonant regions is a large fraction of the total particle speed. This also produces effects that are different from those that would be expected from guiding center considerations and could be associated with some substorm expansions. The guiding center curvature drift term in (1) predicts that j_y will increase if the current sheet becomes thinner and $P_{||} > P_{\perp}$. It therefore is possible for the fewer guiding center particles per unit x length in a thinning current sheet to continue to carry the K_y needed to produce the lobe magnetic field. In contrast, Figure 6 shows that nonguiding center Speiser ions near a resonant region of a thin current sheet already are drifting in the y direction as fast as is practical. A reduced magnetic field line radius of curvature therefore cannot increase V_y much, and the change in κ is likely to reduce V_y in such a region. This fact that V_y/v_0 cannot be increased significantly when it is initially large presents a problem if a thin Speiser current sheet is stretched. The tail particles may not be able to carry the current required to create the lobe field that is needed to balance the solar wind normal force. This process will be most important if κ starts with an initial value of 0.5 and can also be important at higher resonances such as $\kappa = 0.3$ in the more distant tail. It is possible that a sheet can continue thinning until anisotropic guiding center electrons carry enough current. Other possibilities are that the tail shape may change to reduce the local external normal force or the tail could collapse to create a substorm.

A final mechanism that can reduce K_y without decreasing the total number of ions in the tail will be called particle replacement. Field-aligned current between the magnetosphere and the ionosphere is a consequence of the need for charge neutrality. Particle replacement is a mechanism that can reduce the electron contribution to K_y. The process involves precipitation of energetic electrons into the ionosphere and their replacement by low-energy ionospheric electrons. The total number of ions and electrons in the tail remains fixed while the K_y carried by electrons is reduced because low-energy electrons drift slowly in the cross-tail direction. This mechanism is unlikely to be important in a thick current sheet because ions carry most of the cross-tail current. However, electron current could be important on thin sharply curved field lines [*Pritchett and Coroniti*, 1995; *Ma et al.*, 1995; *Birn et al.*, 1996]. The replacement mechanism may be part of a positive feedback effect with precipitation leading to collapse leading to more precipitation. A depletion of the energetic component of magnetotail electrons in a restricted region also could be related to the fading of arcs before substorm onset [*Pellinen and Heikkila*, 1978].

3.3. Causes of Plasma Sheet Thinning

Processes that could produce initial current sheet thinning and therefore a substorm onset by the nonguiding center mechanism are changes in the convection pattern and changes in lobe pressure. It has long been known that the current sheet thickness varies from several Earth radii to about 0.1 R_E while the plasma density changes by a smaller factor. Therefore, although some compression by enhanced z forces is likely and will be considered below, most of the growth phase thinning must involve a removal of plasma from the region of interest [*Hones et al.*, 1971]. The remaining particles then must drift faster across the tail to carry the necessary K_y.

Plasma removal implies an imbalance between sources and sinks. The primary source of plasma sheet particles for the region of interest is inward flow from beyond $x = -20\ R_E$. Most of these particles are likely to start in the magnetosheath and pass through the mantle. Additional contributions come from the flanks and the ionosphere [*Peroomian and Ashour-Abdalla*, 1995]. Plasma is lost from the region of interest through convection toward the Earth and eventually out the dayside magnetopause, through losses at the flanks, through precipitation into the ionosphere, and through drift to open lobe field lines. Since the drift of chaotic particles is different from that of guiding center particles, chaotic orbit effects may be able to enhance this drift to open field lines.

Changes in the interplanetary magnetic field (IMF) are largely responsible for changes in the overall growth phase electric field and associated plasma sheet convection pattern. It is these large-scale convection changes that are likely to be the principal cause of thinning the plasma sheet from several Earth radii down to $< 0.5\ R_E$. For example, the plasma sheet will thin if earthward flow continues at the $x = -14\ R_E$ boundary of our region of interest and decreases at the $x = -20\ R_E$ boundary. Many substorms are triggered by the type of changes in the IMF direction which are likely to produce changes in the convection pattern [*Lyons*, 1996].

A change in the total lobe pressure near $x = -10\ R_E$ also could produce a small change in current sheet thickness in the region of substorm onset. Changes in the solar wind normal force on the magnetopause produce changes in the lobe pressure. Such changes are transmitted at the fast magnetosonic speed to the current sheet near midnight, where onsets are most common. It is this rapid response of the plasma sheet to changes in the solar wind normal force that makes this mechanism interesting. The external force on the magnetopause is determined by the momentum density in the solar wind, by the shape of the magnetopause, and by magnetosheath thermal and magnetic pressures. For example, the magnetopause shape and therefore the normal force are likely to change if the location of dayside merging moves from the subsolar region to a point near the cusps.

The observed increase of K_y in the inner tail before substorms should be associated with some increase in lobe field strength near $x = -10\ R_E$. A very crude estimate of the expected change in the lobe field is $\Delta B_x = (\mu_0 \Delta K_y/2)\ (L_x/R_l)$, where $\Delta K_y/2$ Amperes per meter of additional sheet current closes in the magnetopause of each lobe, L_x is the dimension in the x direction of the region of increased K_y, and R_l is half the thickness of each lobe. This estimate assumes that the added current is localized in a region with $L_x < R_l$. Both B_x and the lobe flux $\pi B_x R_l^2$ should increase. An increase in flux will cause more magnetopause flaring and therefore more normal solar wind force. *Caan et al.* [1975] found such changes in lobe pressure during a substorm cycle but did not plot absolute field magnitudes. *Huang et al.* [1992] and *Kistler et al.* [1993] used total plasma plus field pressure measured in the plasma sheet to estimate the lobe pressure. These latter studies did not find consistent pressure changes during a substorm cycle.

Although changes in lobe pressure which are produced by sudden changes in the solar wind or IMF cannot produce the large changes seen in the thickness of the plasma sheet, they can cause

abrupt thickness perturbations. For example, a 20% increase in the lobe pressure will compress the high-β plasma in the current sheet by about 20%, causing an approximately 10% change in κ for all particles. The change in current sheet thickness and the change in κ could be important if the dominant current carrier orbits are near either the resonant or chaotic limit discussed above.

3.4. 3-D and Time Dependent Processes

Substorms and the diversion of current to the ionosphere are 3-D, time dependent processes. A 2-D model may be appropriate if cross-tail current is disrupted across the tail from flank to flank in a limited x region. However, observations show that disruption usually is limited in both the x and y directions, producing field-aligned currents and a substorm current diversion loop. The COT solutions can be used to study some substorm effects even when the calculations are 2-D and steady state. For example, forces calculated in a 2-D model can provide an estimate of the acceleration expected near the center of a 3-D current diversion loop. The purpose of this section is to examine current continuity as the tail evolves from a 2-D steady state configuration to a 3-D steady state configuration. The final state includes a confined region of reduced V_y/v_o. Small steady field-aligned electron currents also are present in the final configuration.

The $t < t_o$ illustration in Figure 7 shows the initial steady state cross-tail current density $j_y = nqV_{iy}$, the ion bulk drift velocity V_{iy}, and the ion or electron number density n. The magnitudes of these quantities for one fixed x box are plotted along the vertical axis while the horizontal axis is the cross-tail direction with positive y (dusk) to the left. The three plasma parameters have no y dependence at $t < t_o$. Ions drift to the left and electron drift is neglected in all but the $t > t_4$ illustration in Figure 7. No cross-tail electric field or earthward drift is included. It is assumed that a region of reduced V_y/v_o forms instantaneously over a restricted y region at t_o because something changes κ everywhere. The density does not change abruptly at t_o, but ions suddenly begin to drift more slowly and therefore carry less cross-tail current in this localized region. The region of reduced V_{iy} is stationary in all the illustrations, and various structures drift with respect to this fixed region.

Figure 7 is not intended to represent the very complex substorm expansion process. If $j_y(x, z)$ suddenly decreased in a large enough region of the tail, then a substorm could begin as will be discussed in section 4. Here we assume there is only a small decrease in V_{iy} and j_y in a limited region of the tail. In this model the ion density builds up enough by $t = t_4$ so that $j_y = nqV_{iy}$ is the same as the j_y that was present at $t < t_o$.

Any steady state model requires that electron and ion currents must separately be continuous. A transient process involving an increasing particle density requires equal ion and electron currents flowing into a unit volume to maintain charge neutrality [*Atkinson*, 1984]. Since ion cross-tail current drops discontinuously at t_o in a limited y region and we are neglecting cross-tail electron current, a field-aligned electron current must be set up during the transient phase immediately after t_o.

The t_1 illustration of Figure 7 shows the location of the strong field-aligned electron currents that will appear in one to several Alfvén wave bounce periods to close the circuit caused by the discontinuity in cross-tail ion current. This illustration shows the density perturbation that is produced because more ions are entering than leaving the region with a κ associated with chaotic orbits and a small V_{iy}. Ions continue to drift rapidly in the $+y$ direction until they enter the chaotic κ region and resume the rapid drift after they leave the region (Figure 6). The density will increase just enough at

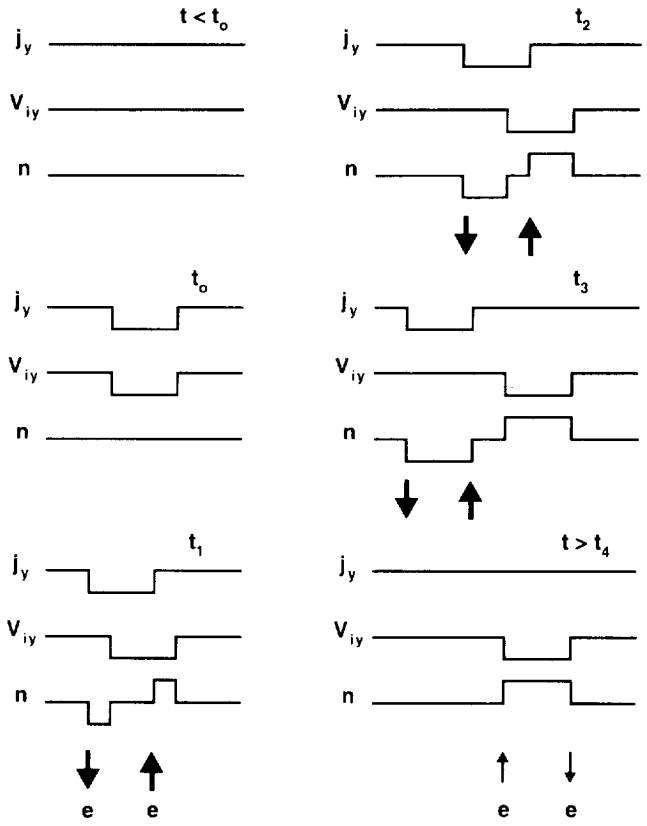

Figure 7. Sketch of a possible time evolution from a steady state two-dimensional (2-D) structure with no y dependence at $t < t_o$ to a steady state 3-D structure at $t > t_4$. The latter structure contains a y region with reduced cross-tail drift speed V_{iy} to show how a confined chaotic κ region could be included in a 3-D COT model. Only ion current is assumed to be significant in the current density j_y, and n is the electron and ion number density. The heavy arrows show the strong field-aligned electron flow that is needed during the transition between steady states. The light arrows show the weak field-aligned electron flow that will be present at the edges of the region of reduced V_{iy} for all $t > t_o$ if the slow electron cross-tail drift is included.

the right side of the region of reduced V_{iy} so that $j_y = nqV_{iy}$ is the same as at $t < t_o$. Ion and electron currents are not separately continuous during this transient stage when the density is changing. As noted above, there is a net cross-tail drift of ions and a net field-aligned drift of electrons into the region of increasing density and out of the region of decreasing density. The heavy arrows in this and following illustrations show the motion of electrons to and from the ionosphere that is required to maintain neutrality. Upgoing ionospheric electrons and their downgoing current connect to the left edge of the region of higher density as this region expands to the left. The total number of ions and electrons in the tail is constant since the density increases in one y region and decreases in another.

The t_2 illustration shows the situation just before the entire reduced V_{iy} region has become filled with the higher-density plasma. The t_3 illustration is still later when the transient region has drifted out of the reduced V_{iy} region. Eventually, the transient region will drift out the dusk flank leaving a new steady state configuration at $t > t_4$. It is only at this time that there will be any change in the total number of ions and electrons in the tail.

If the slow dawnward drift of electrons is included, then the steady state field aligned electron flow indicated by the light arrows

in the $t > t_4$ illustration also will be present. The electrons follow guiding center orbits so electron drift V_{ey} does not change abruptly at the point the ion κ reaches a chaotic value. When cross-tail electron drift is included, these small field-aligned currents will be present at the edges of the reduced V_{iy} region in all but the t_0 panel. The weak field-aligned current is closed by cross-tail electron drift in the higher-density region. It is only the 2-D and 3-D steady state configurations $t < t_0$ and $t > t_4$ that can be modeled using the COT method.

4. Discussion and Summary

4.1. Nonguiding Center Effects

The currents carried by groups of nonguiding center particles were compared to those carried by similarly injected guiding center particles. It was seen that currents carried by the two groups were qualitatively similar but that resonant effects and an energy dependent thickness parameter z_0 were important only for nonguiding center particles. The model magnetic field in the x-y plane is too weak to deflect a nonguiding center particle so that it meanders back and forth across the equatorial plane until it reaches $|z| = z_0$. The 2-D field used here had $B_y = 0$. The z_0 parameter is smaller when a large B_y is added, producing a thinner region of meandering particles.

The most important nonguiding center effects found from the COT analysis involved cross-tail currents in plasmas with anisotropic distribution functions. The frequently used guiding center current equation (1), which is valid when the pressure tensor is described by (3), was found to be inadequate in the inner current sheet. In this region (2), which was derived from the momentum equation and requires knowledge of the full pressure tensor, must be used rather than (1), which involves only $P_{||}$ and $P_{\perp}$. Two specific reasons for the failure of (1) and (3) in the COT current sheet were identified. At $|z| < z_0$ the magnetic field direction was found to be irrelevant to the orientation of the calculated pressure tensor. The pressure tensor became field aligned near $|z| = 1.5\, z_0$. Beyond here a small region was found in which the calculated $\mathbf{P}$ is field aligned but the pressure is dependent upon the azimuthal angle about the magnetic field direction. Equations (1) and (3) could be used only beyond $|z| = 2z_0$ where $\mathbf{P}$ is both field aligned and symmetric about $\mathbf{B}$.

A thick quiet time model field was used for one COT study. This model was selected so that it could to be generated by an isotropic distribution function. As predicted by *Wolf and Pontius* [1993] and *Usadi et al.* [1996], currents were well approximated by (1) in the isotropic current sheet. The distribution functions of each of the separate ion groups, which were combined to produce the COT model, were anisotropic. As a result, (1) did not produce a good approximation to the current carried by individual ion groups, while (2) yielded the correct $j_y(x, z)$ for both individual groups and for the full consistent plasma. A thin current sheet model also was introduced. It was possible to generate a consistent thin current sheet with an anisotropic distribution function using only Speiser particles everywhere except in a region with adiabaticity parameter κ near 0.8.

The above nonguiding center results are important because highly structured distribution functions have been observed in the magnetotail [*Nakamura et al.*, 1991; *Angelopoulos et al.*, 1992; *Frank et al.*, 1996]. Our results suggest that one must evaluate the full pressure tensor to estimate forces in the inner current sheet.

4.2. Substorm Effects

Results from the COT model can be compared to previous analyses of the magnetotail. The *Burkhart et al.* [1992] 1-D simulation is particularly interesting. As in any 1-D study, the $\partial P_{xz}/\partial z$ term generated the x component of particle forces, and the $\partial P_{zz}/\partial z$ term generated the z component. The ion source was located far from $z = 0$, so all particles started on Speiser orbits. As in our case, the off-diagonal pressure tensor element P_{xz} was an order of magnitude smaller than the diagonal element P_{zz}. Forces were well balanced in thin current sheets with small κ.

Burkhart et al. [1992] concluded that solutions could not be found in 1-D simulations when the average κ of injected Speiser orbit ions approached one. Problems were encountered balancing the z components of particle and field forces. The COT method found solutions with κ near one only in thick 2-D current sheets which contained many ions on trapped and cucumber orbits. *Burkhart et al.* [1992] noted that the current sheet tended to become thicker as κ increased from small values even though all ions were injected on Speiser orbits. They concluded that there will be a catastrophic loss of equilibrium if κ slowly increases in a thin current sheet. This is the same effect that is illustrated in Figure 6, where we were unable to find particles with κ near 0.8 that could carry current in a thin sheet. The COT analysis found that other problems can arise in a thinning current sheet which is dominated by resonant particles.

The following sequence of events, suggested by the above findings, may explain why many substorm onsets take place so close to the Earth, near midnight, and in a thin current sheet. A certain lobe field is needed so that the outward force exerted by the lobe on the magnetopause will balance the inward force exerted by the solar wind. A certain electric current is needed in the plasma sheet and magnetopause to generate the required lobe magnetic field. If the current sheet strength decreased in a small region of the tail, it is possible that more current could flow in adjacent regions to generate the lobe field. However, if there are not enough particles or if the particles drift too slowly in a large region of the tail, something more dramatic must happen. A substorm onset which involves the collapse of a segment of the tail is one such dramatic event. Tail collapse will bring more ions into the region with insufficient cross-tail current, will change the thickness of portions of the current sheet, and will change κ and the associated average cross-tail drift speed in the region of interest. The magnetopause shape and therefore the normal force exerted by the solar wind also will change. Another possibility is that guiding center electrons may become the dominant cross-tail current carriers in an extremely thin current sheet [*Pritchett and Coroniti*, 1995; *Ma et al.*, 1995; *Birn et al.*, 1996].

To be more specific, consider the T89 magnetotail which is a widely used model containing a thick current sheet. Assuming that 5-keV protons carry the current in the T89 model, κ is smaller than 0.8 beyond about 12 R_E at midnight, and κ increases away from midnight [*Pulkkinen et al.*, 1992; *Kaufmann et al.*, 1993]. The cross-tail drift speed V_{iy} was found to be strongly dependent on the adiabaticity parameter κ only in thin current sheets which are dominated by particles on Speiser orbits. Our COT analysis found that it is possible to generate thick steady current sheets with $\kappa = 0.8$. The κ parameter decreases as the tail becomes more stretched, B_z decreases, and the current sheet becomes thin. *Burkhart et al.* [1992] and our COT analysis were unable to create a thin steady current sheet with $\kappa = 0.8$.

A substorm therefore would start at whatever location and time the current sheet thickness decreases to $L_z \approx z_0$ and κ of the principal ions also approaches 0.8. This point will be at midnight in T89 because this is the local time at which the current sheet is thinnest and κ is smallest. The onset location will be earthward of 12 R_E if the T89 model correctly describes the magnetotail before thinning begins because κ must initially be larger than 0.8 if it is to decrease to 0.8. Figure 6 also shows that if the current sheet becomes thin, cross-tail drift velocities become small over quite an extended region of the tail, centered at the point $\kappa = 0.8$. *Mitchell et al.* [1990] observed one current sheet that became thin and was dominated by Speiser particles just before a local disruption. *Lui et al.* [1992] found a series of disruptions in data from the AMPTE/CCE satellite which had an apogee of 8.8 R_E. The disruptions took place in current sheets with estimated thicknesses of 0.2 to 0.5 R_E and in regions with estimated adiabaticity parameters of $\kappa = 0.5$ to 0.9.

Some mechanism must reduce the plasma content of the tail as it slowly becomes thin [*Hones et al.*, 1971]. It is generally thought that changes in the electric field or equivalently in the convection pattern are most important during substorm growth phase. A sudden increase in the normal force exerted by the solar wind on the magnetopause could produce a small decrease in plasma sheet thickness. The pressure can respond both to changes in the solar wind momentum density and also to a wide variety of changes in the IMF direction. These small pressure changes could be important because a pressure pulse propagates rapidly to the inner magnetotail near midnight where onsets appear to begin [*Lopez et al.*, 1990; *Lui, et al.*, 1992]. *Lyons* [1996] emphasized how frequently a change in the IMF and the associated convection pattern is associated with substorm onset. The suddenness and localization of substorm onsets and the observation of multiple expansions imply that even triggered substorms involve some internal instability which produces one or a sequence of localized disruptions in the cross-tail current and its diversion to the ionosphere.

Kaufmann et al. [this issue] stressed the possible significance of a net tailward force and the resulting stretching of the plasma sheet everywhere outside a substorm current diversion loop immediately after onset. This process will decrease both κ and the current sheet thickness on the dawnside and duskside of the original diversion loop. Since κ and the current sheet thickness tend to be larger away from midnight, these parameters must both decrease more at the dawn and dusk locations than at midnight in order to reach the $L_z \approx z_0$ and $\kappa \approx 0.8$ values. The stretching after an onset therefore may cause a disruption region that starts near midnight to expand both toward the dawn and dusk. The result could be either a smoothly spreading or a multiple expansion substorm.

The other distinct nonguiding center effect that was discussed also requires a thin current sheet dominated by Speiser orbits. The average nonguiding center particle is already moving along the y axis at nearly its maximum speed in a thin current sheet dominated by Speiser particles with a κ near one of the resonances, such as $\kappa = 0.5$. Unlike guiding center particles, the cross-tail velocity of a resonant particle cannot increase significantly when the current sheet gets still thinner and field lines become more sharply bent. The result again is an inability for ions to carry the current needed to produce the lobe field that must be present to balance the inward force exerted by the solar wind.

The $\kappa = 0.8$ chaotic particle and the $\kappa = 0.5$ resonant particle mechanisms described above both involve a thin current sheet. In both cases the existing ions may be unable to carry the necessary cross-tail current. The principal distinction is that disruption with $\kappa \approx 0.8$ is based on a drop in the average cross-tail velocity. Although the ion content of a section of the tail decreases as the tail becomes thinner [*Hones et al.*, 1971], the $\kappa \approx 0.8$ mechanism is not primarily dependent on a decrease in the total number of ions. In contrast, the $\kappa = 0.5$ mechanism is based upon a loss of plasma from the onset region.

One other mechanism involving electrons which does not require a sudden change in plasma content also was discussed and could contribute to the disruption of cross-tail current. The precipitation of energetic electrons and their replacement by low-energy ionospheric electrons to maintain charge neutrality provides a mechanism that can reduce the electron component of the cross-tail current. The original energetic electrons drift faster and carry more current than the low-energy replacement electrons.

The COT calculations assume steady state conditions, and those presented here were two-dimensional. A qualitative discussion of ways in which these results could fit into a 3-D time dependent substorm model was included. This was primarily a time dependent extension of the current diversion process discussed by *Kaufmann et al.* [1994]. The specific example considered was an evolution from one steady state condition to another. It was seen that ion and electron currents each are continuous in a steady state model. Electrons carry small steady field-aligned currents at the edges of a region of high or low density that is confined in the cross-tail direction. These currents are closed by cross-tail electron drift near the equator. Electron and ion currents are not individually continuous during the transient period in which the plasma density is increasing or decreasing. This situation requires equal net electron and ion currents to flow into or out of the region of changing density [*Atkinson*, 1984]. The result is a large field-aligned electron current which provides continuity during the transient phase when combined with the discontinuous ion cross-tail current.

Many other mechanisms could produce substorm onset in a thin current sheet but were not discussed because they have been reviewed recently [*Baker et al.*, 1996; *Birn et al.*, 1996; *Lui*, 1996; *Lyons*, 1996; *Rostoker*, 1996; *Sergeev et al.*, 1996]. The nonguiding center mechanisms discussed here are speculative. However, they require a specific current sheet thickness of about $2z_0$, an anisotropic distribution function dominated by Speiser particles, and either κ near 0.8 or κ near a resonance (e.g., $\kappa = 0.5$) with large V_y/v_0 and so should be testable.

Acknowledgments. The reviewers made a number of constructive suggestions that were added to the manuscript. This material is based upon work supported by the National Science Foundation under grant ATM-94-22056 and by the National Aeronautics and Space Administration under grants NAGW-4539 and NAG5-4453.

The Editor thanks two referees for their assistance in evaluating this paper.

References

Angelopoulos, V., W. Baumjohann, C. F. Kennel, F. V. Coroniti, M. G. Kivelson, R. Pellat, R. J. Walker, H. Lühr, and G. Paschmann, Bursty bulk flows in the inner central plasma sheet, *J. Geophys. Res.*, *97*, 4027-4039, 1992.

Atkinson, G., Field-aligned currents as a diagnostic tool: Result, a renovated model of the magnetosphere, *J. Geophys. Res.*, 89, 217-226, 1984.

Baker, D. N., T. I. Pulkkinen, V. Angelopoulos, W. Baumjohann, and R. L. McPherron, Neutral line model of substorms: Past results and present view, *J. Geophys. Res.*, *101*, 12,975-13,010, 1996.

Birn, J., R. Sommer, and K. Schindler, Open and closed magnetospheric tail

configurations and their stability, *Astrophys. Space Sci.*, *35*, 389-402, 1975.

Birn, J., M. Hesse, and K. Schindler, MHD simulations of magnetotail dynamics, *J. Geophys. Res.*, *101*, 12,939-13,954, 1996.

Büchner, J., and L. M. Zelenyi, Regular and chaotic charged particle motion in magnetotaillike field reversals, 1, Basic theory of trapped motion, *J. Geophys. Res.*, *94*, 11,821-11,842, 1989.

Burkhart, G. R., J. F. Drake, P. B. Dusenbery, and T. W. Speiser, A particle model for magnetotail neutral sheet equilibria, *J. Geophys. Res.*, *97*, 13,799-13,815, 1992.

Caan, M. N., R. L. McPherron, and C. T. Russell, Substorm and interplanetary magnetic field effects on the geomagnetic tail lobes, *J. Geophys. Res.*, *80*, 191-194, 1975.

Cole, G. H. A., and K. Schindler, On the equilibrium configuration of the geomagnetic tail, *Cosmic Electrodyn.*, *3*, 275-284, 1972.

Cowley, S. W. H., The effect of pressure anisotropy on the equilibrium structure of magnetic current sheets, *Planet. Space Sci.*, *26*, 1037-1061, 1978.

Frank, L. A., W. R. Paterson, K. L. Ackerson, S. Kokubun, and T. Yamamoto, Plasma velocity distributions in the near-Earth plasma sheet: A first look with the Geotail spacecraft, *J. Geophys. Res.*, *101*, 10,627-10,637, 1996.

Hill, T. W., and G. -H. Voigt, Limits on plasma anisotropy in a tail-like magnetic field, *Geophys. Res. Lett.*, *19*, 2441-2444, 1992.

Hones, E. W., Jr., J. R. Asbridge, and S. J. Bame, Time variations of the magnetotail plasma sheet at 18 R_E determined from concurrent observations by a pair of vela satellites, *J. Geophys. Res.*, *76*, 4402-4419, 1971.

Huang, C. Y., L. A. Frank, G. Rostoker, J. Fennell, and D. G. Mitchell, Nonadiabatic heating of the central plasma sheet at substorm onset, *J. Geophys. Res.*, *97*, 1481-1495, 1992.

Kaufmann, R. L., and C. Lu, Cross-tail current: Resonant orbits, *J. Geophys. Res.*, *98*, 15,447-15,465, 1993.

Kaufmann, R. L., D. J. Larson, P. Beidl, and C. Lu, Mapping and energization in the magnetotail, 1, Magnetospheric boundaries, *J. Geophys. Res.*, *98*, 9307-9320, 1993.

Kaufmann, R. L., C. Lu, and D. J. Larson, Cross-tail current, field-aligned current, and B_y, *J. Geophys. Res.*, *99*, 11,277-11,295, 1994.

Kaufmann, R. L., D. J. Larson, I. D. Kontodinas, and B. M. Ball, Force balance and substorm effects in the magnetotail, *J. Geophys. Res.*, this issue.

Kistler, L. M., W. Baumjohann, T. Nagai, and E. Möbius, Superposed epoch analysis of pressure and magnetic field configuration changes in the plasma sheet, *J. Geophys. Res.*, *98*, 9249-9258, 1993.

Larson, D. J., and R. L. Kaufmann, Structure of the magnetotail current sheet, *J. Geophys. Res.*, *101*, 21,447-21,461, 1996.

Lopez, R. E., D. G. Sibeck, R. W. McEntire, and S. M. Krimigis, The energetic ion substorm injection boundary, *J. Geophys. Res.*, *95*, 109-117, 1990.

Lui, A. T. Y., Current disruption in the Earth's magnetosphere: Observations and models, *J. Geophys. Res.*, *101*, 13,067-13,088, 1996.

Lui, A. T. Y., R. E. Lopez, B. J. Anderson, K. Takahashi, L. J. Zanetti, R. W. McEntire, T. A. Potemra, D. M. Klumpar, E. M. Greene, and R. Strangeway, Current disruptions in the near-Earth neutral sheet region, *J. Geophys. Res.*, *97*, 1461-1480, 1992.

Lyons, L. R., Substorms: Fundamental observational features, distinction from other disturbances, and external triggering, *J. Geophys. Res.*, *101*, 13,011-13,025, 1996.

Ma, Z. W., X. Wang, and A. Bhattacharjee, Growth, sudden enhancement, and relaxation of current sheets in the magnetotail: Two-dimensional substorm dynamics, *Geophys. Res. Lett.*, *22*, 2985-2988, 1995.

Mitchell, D. G., D. J. Williams, C. Y. Huang, L. A. Frank, and C. T. Russell, Current carriers in the near-Earth cross-tail current sheet during substorm growth phase, *Geophys. Res. Lett.*, *17*, 583-586, 1990.

Nakamura, M., G. Paschmann, W. Baumjohann, and N. Sckopke, Ion distributions and flows near the neutral sheet, *J. Geophys. Res.*, *96*, 5631-5649, 1991.

Nötzel, A., K. Schindler, and J. Birn, On the cause of approximate pressure isotropy in the quiet near-Earth plasma sheet, *J. Geophys. Res.*, *90*, 8293-8300, 1985.

Ohtani, S., K. Takahashi, L. J. Zanetti, T. A. Potemra, R. W. McEntire, and T. Iijima, Initial signatures of magnetic field and energetic particle fluxes at tail reconfiguration: Explosive growth phase, *J. Geophys. Res.*, *97*, 19,311-19,324, 1992.

Parker, E. N., Newtonian development of the dynamical properties of ionized gases of low density, *Phys. Rev.*, *107*, 924-933, 1957.

Pellinen, R. J., and W. J. Heikkila, Observations of auroral fading before breakup, *J. Geophys. Res.*, *83*, 4207-4217, 1978.

Peroomian, V., and M. Ashour-Abdalla, Relative contribution of the solar wind and the auroral zone to near-Earth plasmas, in *Cross-Scale Coupling in Space Plasmas*, *Geophys. Monogr. Ser.*, vol. 93, edited by J. L. Horwitz, N. Singh, and J. L. Burch, pp. 213-217, AGU, Washington, D. C., 1995.

Pritchett, P. L, and F. V. Coroniti, Formation of thin current sheets during plasma sheet convection, *J. Geophys. Res.*, *100*, 23,551-23,565, 1995.

Pulkkinen, T. I., D. N. Baker, R. J. Pellinen, J. Büchner, H. E. J. Koskinen, R. E. Lopez, R. L. Dyson, and L. A. Frank, Particle scattering and current sheet stability in the geomagnetic tail during the substorm growth phase, *J. Geophys. Res.*, *97*, 19,283-19,297, 1992.

Rich, F. J., V. M. Vasyliunas, and R. A. Wolf, On the balance of stresses in the plasma sheet, *J. Geophys. Res.*, *77*, 4670-4676, 1972.

Rossi, B., and S. Olbert, *Introduction to the Physics of Space*, McGraw-Hill, New York, 1970.

Rostoker, G., Phenomenology and physics of magnetospheric substorms, *J. Geophys. Res.*, *101*, 12,955-12,973, 1996.

Sergeev, V. A., T. I. Pulkkinen, and R. J. Pellinen, Coupled-mode scenario for the magnetospheric dynamics, *J. Geophys. Res.*, *101*, 13,047-13,065, 1996.

Speiser, T. W., Particle trajectories in model current sheets, 1, Analytic solutions, *J. Geophys. Res.*, *70*, 4219-4226, 1965.

Tsyganenko, N. A., A magnetospheric magnetic field model with a warped tail current sheet, *Planet. Space Sci.*, *37*, 5-20, 1989.

Tsyganenko, N. A., and A. V. Usmanov, Determination of the magnetospheric current system parameters and development of experimental geomagnetic field models based on data from IMP and HEOS satellites, *Planet. Space Sci.*, *30*, 985-998, 1982.

Usadi, A., R. A. Wolf, M. Heinemann, and W. Horton, Does chaos alter the ensemble averaged drift equations?, *J. Geophys Res.*, *101*, 15,491-15,514, 1996.

Wolf, R. A., and D. H. Pontius Jr., Particle drift in the Earth's plasma sheet, *Geophys. Res. Lett.*, *20*, 1455-1458, 1993.

Zwingmann, W., Self-consistent magnetotail theory: Equilibrium structures including arbitrary variation along the tail axis, *J. Geophys. Res.*, *88*, 9101-9108, 1983.

B. M. Ball, R. L. Kaufmann, I. D. Kontodinas, and D. J. Larson, Department of Physics, University of New Hampshire, Durham, NH 03824-3568. (e-mail: dick.kaufmann@unh.edu)

(Received April 21, 1997; revised July 2, 1997;
accepted July 9, 1997.)